Full length article

Effect of swirl on premixed flame response at high forcing amplitudes

Dimitrios P. Kallifronas [a,*], James C. Massey [a,b], Zhi X. Chen [a,1], Ramanarayanan Balachandran [c], Nedunchezhian Swaminathan [a]

[a] Department of Engineering, University of Cambridge, Trumpington Street, Cambridge CB2 1PZ, United Kingdom
[b] Robinson College, University of Cambridge, Grange Road, Cambridge CB3 9AN, United Kingdom
[c] Department of Mechanical Engineering, University College London, Torrington Place, London WC1E 7JE, United Kingdom

ARTICLE INFO

ABSTRACT

The response of a lean premixed flame subjected to acoustic perturbations is a complex phenomenon that depends highly on the type of flame and the operating conditions. Swirl introduces additional complexities due to the azimuthal component of the flow. In this work, a bluff body stabilised burner is studied under non-swirling and highly swirling conditions by placing a removable axial swirl upstream of the burner. The influence of swirl is assessed in terms of the flame describing function which is the ratio of heat release rate fluctuations response to incoming velocity oscillations and the spatial flame dynamics at high forcing amplitudes. The effect of flame interaction with the wall on the flame response is also explored by considering an enclosure with a larger diameter. It is found that swirl can affect the non-linear characteristics of the flame at medium frequencies (Strouhal numbers around unity) by altering the flame roll-up mechanisms. This is related to the variation of the local swirl number in space and time. For Strouhal numbers that are considerably lower than unity, the effect of swirl is small due to the high convective wavelengths. The size of the enclosure can also change the flame response characteristics, specifically for large forcing frequencies. With a small enclosure, where the flame interacts with the wall, the flame break-up is more significant and the vortex formation is interrupted. This does not happen when the enclosure is enlarged and it can affect the non-linear behaviour of the flame.

1. Introduction

Lean premixed flames emit low levels of NO_x and hence they are of great interest to practical systems such as gas turbines. However, these flames are prone to combustion instabilities which can cause significant structural damage to the system, if the instabilities are uncontrolled. These instabilities arise through the interaction between heat release rate and pressure fluctuations and they manifest through tonal noise (acoustic pressure fluctuation at selected and discrete frequencies). Combustion system geometry plays an important role in the manifestation of these thermo-acoustic instabilities. Low-order acoustic network models are commonly used to study dominant modes and limit cycle amplitudes of these instabilities in a given combustor [1–3]. Invariably, these models need an appropriate Flame Describing Function (FDF) as an input. This function denoted by H is defined as the ratio of the heat release rate fluctuation, $\dot{Q}'$, to velocity fluctuations u' both normalised appropriately and it is written as [4,5]

$$H(f, |u'|) = \frac{\dot{Q}'(f, |u'|)/\langle \dot{Q} \rangle}{|u'|/\langle u \rangle}, \tag{1}$$

where $\langle \dot{Q} \rangle$ is the time-averaged value of volume integrated heat release rate $\dot{Q}(t) = \int_{V_c} \dot{q}(\mathbf{x}, t)dV$ with V_c as the combustor volume and $\dot{q}$ as the local heat release rate per unit volume at a given location $\mathbf{x}$ and time t. The fluctuating heat release rate is $\dot{Q}' = \dot{Q} - \langle \dot{Q} \rangle$. The FDF is a function of both frequency and forcing (velocity) amplitude and it assumes that the dominant frequency of the flame response is the same as that of the flow perturbations arising from acoustic forcing.

There is a wealth of information on the FDF for non-swirling flames and non-linear analytical models developed in earlier studies [6–8] assumed that flame response saturated above a certain velocity (forcing) amplitude. Schuller et al. [4] observed that V-flames with large angles with respect to mean flow (flatter flames) had reduced sensitivity to flow perturbations while those with small angle (longer flames) showed higher sensitivity. This is because of the flame area changes induced by convective effects are more significant in longer flames. These non-linear effects can be included in low-order acoustic model to investigate growth rates of perturbations to understand combustor stability as has been done in past studies [3,9–11].

The significance of flame surface modulations as the main source of heat release rate oscillations and the flame roll-up as the source of non-linearity were highlighted in past experimental studies [5,12]. The experiments of Balachandran et al. [5] have been investigated numerically using unsteady Reynolds-averaged Navier–Stokes (URANS) calculations [13,14] and large eddy simulations (LES) [3,15–17] confirming the experimental observations, specifically the flame roll-up on the saturation of heat release rate response.

Understanding the FTF behaviour of swirling flames is significantly more challenging since local maxima and minima are common as the forcing frequency changes. A large number of past studies have focused on that behaviour at a single forcing amplitude [18–21] or at multiple amplitudes but with limited discussion on saturation and the flame behaviour at higher amplitudes [22–25]. Bellows et al. [26] and Liu et al. [27] have elaborated further on the behaviour of swirling flames at high amplitudes and found that a second linear region at high forcing amplitudes is not uncommon. Bellows et al. [26] also described how saturation occurs due to vortex roll-up at lower frequencies while flame lift-off is prevalent at higher forcing frequencies. For partially premixed flames, Rajendram-Soundararajan et al. [28] observed that increasing swirl saturated the response of partially premixed flames at large forcing frequencies for the range of amplitudes, up to $A = u'/\langle u \rangle \approx 0.35$. However, those three studies [26–28] considered only swirling flames. Therefore, to the authors' best knowledge, there have been no studies where the response of non-swirling and swirling flames at high forcing amplitudes has been compared with emphasis on the flame dynamics.

A narrow enclosure around a flame will affect the flame angle, height and the convective speed (thus convective time delay). Also, the flame is likely to interact with the enclosure and thus the confinement has an important effect on the flame response. A change in the convective timescale can alter the FDF gain behaviour by shifting its peak to higher frequencies in both laminar [29,30] and turbulent swirling flames [31]. Also, the flame shapes and dynamics may differ when a single or multiple burners are used because of dilatation effects [30] and these effects can be severe in a confined environment. Hence understanding the effect of confinement on the FDF and flame dynamics is important and this information is scarce in the open literature.

Furthermore, another important aspect which could influence flame shape and dynamics is the heat loss through the combustor (enclosure) walls. It has been observed that a V-shaped flame can change to M-shaped flame under fixed flow conditions when the heat losses are small and an M-shaped flame can have a broader frequency response in terms of flame dynamics [12,29]. However, the gain of the FDF is not influenced significantly by the heat losses but its phase can be different as observed by Cheng et al. [17] in their LES. The flame response is delayed under adiabatic conditions which leads to some under estimates in the FDF phase, particularly in the non-linear regime. Having said all of these, one must recognise that specifying the wall temperature or heat loss through the walls in LES is challenging unless these quantities are characterised well in the experiments, which is uncommon.

The first objective here is to conduct LES of swirling and non-swirling bluff body stabilised premixed flames and compare the findings to experimental results. The LES results are to be used to understand and compare the physical mechanisms responsible for the non-linearities in the two types of flames at high forcing amplitudes. The second objective is to study confinement effects on the FDF by considering a narrow (as in the experiments [32]) and a wider (only for the computational model) flame enclosure. The rest of this paper is arranged as follows. The flame configuration investigated experimentally [32] is described briefly in the next section along with its computational model used for LES. The results are discussed in Section 4 and conclusions are summarised in the final section.

2. Burner details

Fig. 1 shows a schematic of the flame and burner configuration used for this study. The combustor is cylindrical with a diameter of 70 mm and a height of $L = 80$ mm as shown in the figure. The conical bluff body having a blockage ratio of 50% has a base diameter of $D_0 = 25$ mm and 45° angle, which acts as the flame holder. For the swirling cases, an axial swirler with six flat vanes positioned at 60° angle with respect to the flow and 13.6 mm high is placed at 50 mm upstream of the bluff body base (dump plane) as shown in the figure. Since the turbulence inside the combustor is dominated by the shear-driven (in non-swirling case) and the swirler wake generated turbulence, there is no perforated plate or turbulence grid in the experimental setup [32]. The bulk-mean velocity of the premixed ethylene-air mixture at the dump plane is $u_0 = 10$ m/s for both the swirling and non-swirling cases. The equivalence ratio, ϕ, of this mixture is 0.55 for the non-swirling and 0.52 for the swirling cases [32]. The swirl number defined as the ratio of azimuthal to axial momentum fluxes at the dump plane and calculated using [33]

$$SN = \frac{\int_0^{R_p} u_x u_\theta r^2 \, dr}{R_p \int_0^{R_p} u_x^2 r \, dr} \tag{2}$$

is $SN = 0.97$, where $R_p = 17.5$ mm is the radius of the inlet pipe. It is worth noting that the small change in ϕ between the non-swirling and swirling cases causes the unstrained laminar flame speed to drop by about 20%, which must be borne in mind while comparing results of these two cases. Hot-wire anemometer was used [32] to measure u_0 and a two microphone method was used to capture the velocity fluctuations. The two microphones are mounted 125 and 365 mm upstream of the dump plane. To record the flame response to acoustic forcing, OH* and CH* were used . The OH planar laser induced fluorescence (PLIF) was used to obtain the flame surface density (FSD). More details on the experiments, diagnostics used can be found in [32].

A third case with the same swirler but a wider enclosure (diameter of 70 mm increased to 100 mm) is also considered only for LES to study the confinement effects on the flame response. These three, non-swirling, swirling and swirling with a larger enclosure, cases are respectively called as S0, S60, and S60L respectively in the discussion below.

3. Numerical modelling

3.1. LES model

The compressible, Favre-filtered transport equations for mass, momentum and energy (total enthalpy h) are solved for large eddy simulation. These equations for mass and momentum are, respectively,

$$\frac{\partial \overline{\rho}}{\partial t} + \frac{\partial \overline{\rho} \widetilde{u}_j}{\partial x_j} = 0, \quad \text{and} \tag{3}$$

$$\frac{\partial \overline{\rho} \widetilde{u}_i}{\partial t} + \frac{\partial \overline{\rho} \widetilde{u}_i \widetilde{u}_j}{\partial x_j} = \frac{\partial \overline{p}}{\partial x_i} + \frac{\partial \overline{\tau}_{ij}}{\partial x_j} - \frac{\partial (\overline{\rho u_i u_j} - \overline{\rho} \widetilde{u}_i \widetilde{u}_j)}{\partial x_j}, \tag{4}$$

where ρ is the mixture density, u_i the velocity component in direction i, p the pressure and τ_{ij} the molecular shear stress. The residual stress tensor $(\overline{\rho u_i u_j} - \overline{\rho} \widetilde{u}_i \widetilde{u}_j)$ is calculated using the dynamic Smagorinsky model [34,35], which is written as

$$\nu_T = (C_S \Delta)^2 \sqrt{2 \widetilde{S}_{ij} \widetilde{S}_{ij}}, \tag{5}$$

where Δ is the LES filter width and $\widetilde{S}_{ij}$ is the filtered symmetric strain rate tensor. The dynamic model constant is C_S.

The local thermo-chemical condition of the reacting mixture is described using two-variable formulation and these variables are the mixture fraction, describing the local mixing conditions, and a reaction progress variable to describe the progress of chemical reactions. Thus,
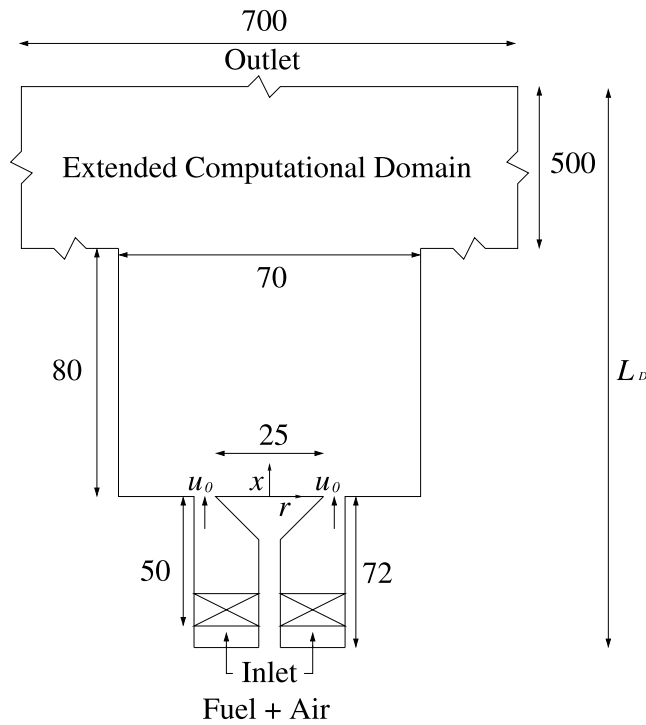
Fig. 1. Schematic of the bluff body burner [32] used for this study.

transport equations for the Favre-filtered mixture fraction, $\widetilde{\xi}$, reaction progress variable, $\widetilde{c}$, and their sub-grid variance, $\sigma_{c,\text{sgs}}^2$ and $\sigma_{\xi,\text{sgs}}^2$, are solved. Since the system considered for this study is fully premixed the mixture fraction variance is excluded and also $\widetilde{\xi}$ is used to track the mixing of hot gases exiting the combustor with the ambient air inside the extended computational domain (see Fig. 1). This extended domain is included to specify clean outlet boundary conditions since the flame may extend beyond the combustor of height 80 mm.

The mixture fraction is defined using Bilger's formula [36] and the progress variable is defined as $c = (Y_{\text{CO}} + Y_{\text{CO}_2})/(Y_{\text{CO}} + Y_{\text{CO}_2})_b$ with subscript b denoting the burnt condition. The progress variable increases monotonically from zero in the reactants to unity in the burnt products. The transport equations for the additional quantities and total enthalpy, h, are written in a compact form using $\widetilde{\varphi} = \{\widetilde{h}, \widetilde{c}, \sigma_{c,\text{sgs}}^2, \widetilde{\xi}\}^\top$, as

$$\frac{\partial \overline{\rho}\widetilde{\varphi}}{\partial t} + \frac{\partial}{\partial x_j}\left(\overline{\rho}\widetilde{u}_j\widetilde{\varphi}\right) = \frac{\partial}{\partial x_j}\left(\overline{\rho}\widetilde{D}_{\text{eff}}\frac{\partial \widetilde{\varphi}}{\partial x_j}\right) + \overline{S_\varphi^+} - \overline{S_\varphi^-}. \tag{6}$$

The effective diffusivity is $\widetilde{D}_{\text{eff}} = D_\varphi + \nu_t/Sc_t$, where ν_t is the sub-grid eddy viscosity and D_φ is the molecular diffusivity for φ which is taken to be the thermal diffusivity, α, for the enthalpy. For the other scalars, $D_\varphi \equiv \nu/Sc$, where $Sc = 0.7$ is the molecular Schmidt number. The turbulent Prandtl, Pr_t and Schmidt, Sc_t, numbers are set to be 0.4 following earlier studies [37,38]. The filtered temperature is obtained from the transported enthalpy using $\widetilde{T} = T_0 + \left(\widetilde{h} - \widetilde{\Delta h}_f^0\right)/\widetilde{c}_p$ where $\widetilde{\Delta h}_f^0$ and $\widetilde{c}_p$ are respectively the enthalpy of formation and specific heat capacity of the mixture, and $T_0 = 298.15$ K. The fluid density is obtained using the state equation. The sources $\overline{S_\varphi^+}$ and sinks $\overline{S_\varphi^-}$ in Eq. (6) are respectively written as

$$\overline{S_\varphi^+} = \left\{\frac{D\overline{p}}{Dt}, \overline{\dot{\omega}}_c, 2\overline{\rho}\frac{\nu_T}{Sc_T}|\nabla\widetilde{c}|^2 + 2\left(\overline{c\,\dot{\omega}_c} - \widetilde{c}\,\overline{\dot{\omega}}_c\right), 0\right\}^\top, \tag{7}$$

$$\overline{S_\varphi^-} = \left\{0, 0, 2\overline{\rho}\,\widetilde{\chi}_{c,\text{sgs}}, 0\right\}^\top. \tag{8}$$

The subgrid scalar dissipation rate (SDR), $\widetilde{\chi}_{c,\text{sgs}}$, is calculated using the algebraic model of Dunstan et al. [39]. The filtered reaction rate,

$\overline{\dot{\omega}}_c$, is obtained using a presumed probability density function (PDF) approach [38,40–42]:

$$\overline{\dot{\omega}}_c = \overline{\rho}\int_0^1 \frac{\dot{\omega}_c(\zeta)}{\rho(\zeta)}\,\widetilde{P}(\zeta)\,d\zeta, \tag{9}$$

where $\dot{\omega}_c(\zeta) = (\dot{\omega}_{\text{CO}} + \dot{\omega}_{\text{CO}_2})/(Y_{\text{CO}} + Y_{\text{CO}_2})_b$ and $\rho(\zeta)$ are the flamelet reaction rate and mixture density respectively. The density-weighted PDF is approximated using a β-distribution for specified values of $\widetilde{c}$ and $\sigma_{c,\text{sgs}}^2$ which are obtained using their respective transport equations. However, a look-up table for the filtered reaction rate can be constructed before the LES is started since the ranges of $\widetilde{c}$ and $\sigma_{c,\text{sgs}}^2$ are well defined. Hence, premixed flamelets (unstrained laminar premixed flames) having desired thermo-chemical and thermo-physical conditions are calculated using Cantera [43]. Ethylene-air mixtures at NTP having equivalence ratios of 0.55 and 0.52 are of interest for this study. The combustion chemistry is modelled using USC chemical mechanism involving 529 elementary reactions and 75 species [44]. The source term $\overline{c\,\dot{\omega}_c}$ required for $\sigma_{c,\text{sgs}}^2$ is calculated using an equation similar to Eq. (9). The other thermochemical quantities such as mixture's specific heat capacity, molecular weight, etc., required during the turbulent combustion simulations (LES) are also precomputed and stored in the look-up table as has been done in past studies [38,40–42].

3.2. Computational details

Unstructured meshes having tetrahedral cells of total count between 2.3 and 2.9 million are used for the 3 cases, S0, S60 and S60L. The mesh for case S60 can be seen in Fig. 2. The entire swirler geometry is included in the mesh for the swirling cases, S60 and S60L. The grid size and distribution are chosen based on a mesh sensitivity study for S60 and this grid distribution is used for the other two cases to maintain a consistency and some basis for meaningful comparison of results. As noted earlier, an extended cylindrical domain with a diameter of 700 mm and height of 500 mm is added at the combustor exit, see Fig. 2, so that the numerical conditions at the outlet can be specified unambiguously since the flame was observed to extend beyond the combustor height of 80 mm in the experiments. Spatial derivative are discretised using second order numerical schemes and the discretised equations are time advanced using a first order implicit Euler scheme available in the open-source package OpenFOAM 7. A modified PIMPLE algorithm is used with density coupling to handle compressibility effects (rhoPimpleFoam solver).

The adiabatic walls are specified to be no-slip and wall functions are used to capture the near-wall flow following earlier studies [45,46]. A constant mean velocity with synthetically generated turbulence having an intensity of 5% is prescribed at the computational inlet boundary. A sinusoidal velocity variation without altering the mean value is superimposed on the prescribed velocity to mimic the acoustic forcing. A wave transmissive boundary condition is used for pressure at the computational domain outlet.

The statistics are collected over a period of $10\tau_f$ after allowing $3\tau_f$ for initial transients to escape the domain in unforced flames, where $\tau_f = L_D/u_0$ is the flow through time for the entire computational domain. At least 25 forcing cycles, after allowing the initial transients to escape, are considered to collect the data required to construct FDF and phase-averaged statistics in forced flames. These simulations are performed using the ARCHER2 UK national high performance computing facility.

The forcing amplitudes are characterised using a two-microphone method in the experiments [32]. This characterisation is also calibrated using a hotwire aneamometer at the dump-plane. Hence, the velocity amplitude at the dump-plane is used to denote the forcing amplitude in the LES. However, the influence of physical presence of the swirler on this approach is yet to be investigated in detail, which will be reported in a future study.
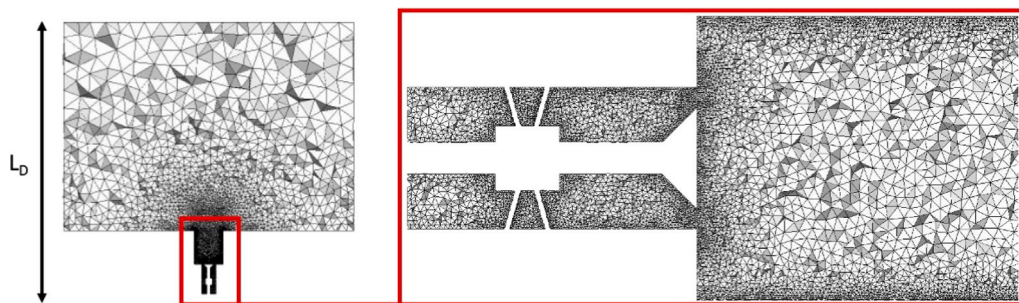
Fig. 2. The numerical grid used for case S60 for LES is shown in the mid-plane of the computational domain.
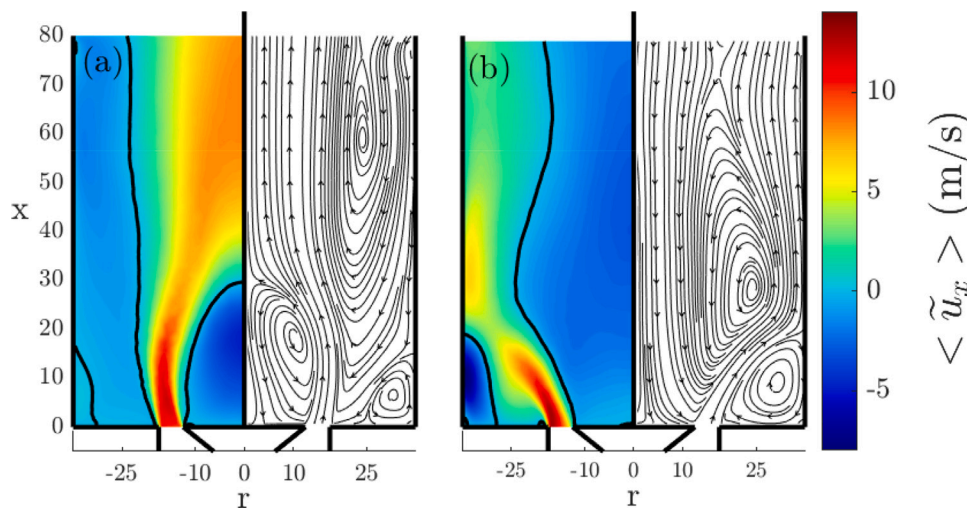

Fig. 3. Computed axial velocity contours and streamline patterns for cases (a) S0 and (b) S60. The black lines in the left halves denote zero axial velocity. Dimensions are in mm.

4. Results and discussion

4.1. Validation

Fig. 3a and b show the flow structure in S0 (no swirl) and S60 (swirling) cases under isothermal conditions. The left halves show the axial velocity and the streamlines are shown in the right halves. The presence of the central recirculation zone (CRZ) behind the bluff body is seen clearly for S0 case and this single toroidal vortex extends up to about $x = 30$ mm which is $1.2D_0$. There is a long side recirculation zone (SRZ) extending beyond 80 mm but the outer recirculation zone (ORZ) is relatively small. On the other hand, the ORZ is larger in the swirling case, the jet impinges on the combustor wall, and the main recirculation zone (merged SRZ and CRZ) extends outside the combustor due to the high level of swirl. The absence of a vortex breakdown bubble (VBB) and the long CRZ suggest that the VBB has merged with the CRZ forming a single recirculation region. This is expected for this high swirl and leads to the formation of a highly unsteady CRZ, its size and shape varying in time as observed in [46].

Fig. 4 compares the azimuthally averaged mean and rms values of axial and radial velocities with Laser Doppler Velocimetry (LDV) measurements. These results are shown for S0 at three axial locations and the agreement is very good for the mean velocities. The rms velocities near the shear layers are underestimated as has been observed in past studies [15,47], but this does not affect the estimation of the FDF unduly as one shall see later. It is unfortunate that there are no measurements reported for S60 and hence a comparison is not shown here. However, this computational model was validated extensively in a past study [46] for both non-reacting and reacting flows in a similar burner.

Fig. 5 compares the computed and measured flame brush (time-averaged flame) shapes for cases S0 and S60 using FSD, Σ. This quantity for LES is calculated using the formula:

$$\Sigma = \frac{\dot{q}}{\Delta H_c \rho_u s_l} = \frac{\overline{\dot{\omega}}_c Y_{f,u}}{\rho_u s_l} \tag{10}$$

where $\dot{q}$ is the local heat release rate per unit volume, ΔH_c is the lower calorific value of ethylene, ρ_u is the unburnt mixture density, s_l is the unstrained laminar flame speed and $Y_{f,u}$ is the fuel mass fraction in the unburnt mixture. The FSD for the experimental flames is obtained using OH-PLIF images as described in [5]. The computed flame brush shapes compare well for the non-swirling case S0 shown in Fig. 5a. The highest reaction rate in the LES is seen near the base which is consistent with the experiment. There is also another region of high reaction rate near the tip. The computed height of the flame brush L_f is approximately 59 mm $(2.4D_0)$ which compares well with measurements. The LES flame height is assumed to be the maximum height of the $\tilde{c} = 0.9$ iso-contour. However, the adiabatic walls specified for LES yield a stronger outer flame, specifically near the base, compared to the experiment and also the stronger dilatation effects near the side wall pushes the flame brush towards the centre compared to the measurement.

The flame brush shape in the S60 case shown in Fig. 5b is considerably different compared to S0. The flame brush is thicker near the base and the peak value of FSD is lower compared to S0. Also, the flame brush is shorter, approximately 48 mm $(1.9D_0)$ in the S60 case. The heat release rate is distributed evenly and some flame flattening is observed near the tip suggesting flame-wall interaction. This increases the heat losses in the swirling case. The computed and measured flame brushes agree quite well.

The flame is located along the shear layer in both cases but it is compact in the swirling case and experiences higher turbulence.
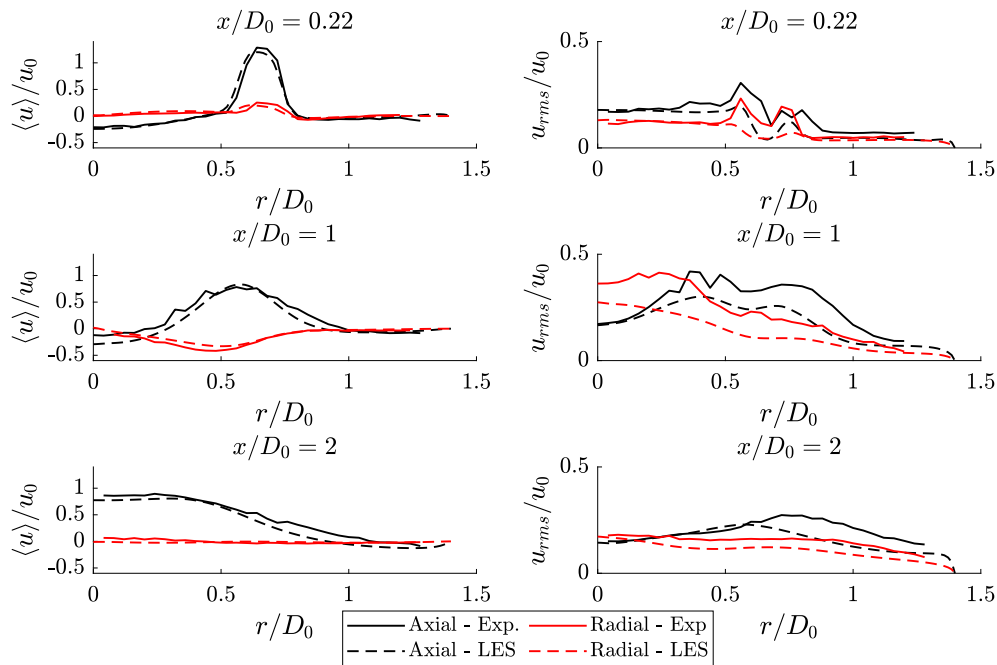
Fig. 4. Mean and rms velocity profiles for case S0.
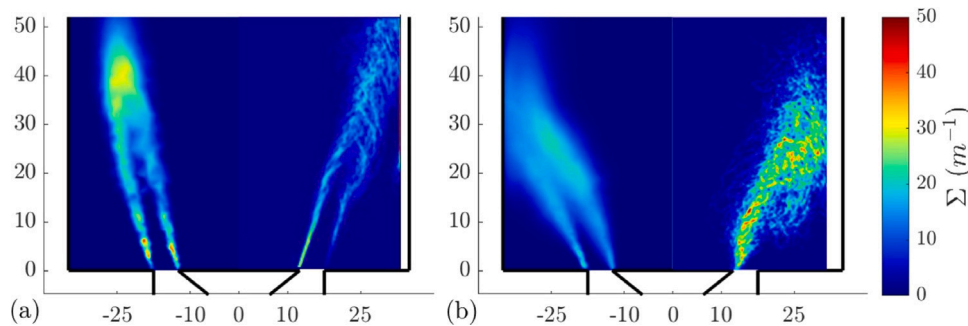*Source:* Measurements obtained from [32].

Fig. 5. The shape of measured (right halves) and computed (left) flame brush in cases (a) S0 and (b) S60.

Hence, it is expected to be unsteadier compared to S0. Indeed, this is seen clearly from the results shown in Fig. 6. The time series of volume-integrated heat release rate, calculated as

$$\dot{Q} = \Delta H_c \int_{V_c} \dot{\omega}_f \; dV, \tag{11}$$

where $\dot{\omega}_f$ is the local fuel consumption rate per unit volume, is shown in Fig. 6a for S0 and S60 cases. The time-averaged heat release rate in the S60 flame is slightly lower (by about 8%) because of its lower equivalence ratio (0.52) compared to the S0 case (0.55). However, the fluctuations are significantly larger in the swirling case with a peak-to-peak amplitude of about 10% while it is around 2% for the non-swirling flame. Despite these fluctuations, both flames have very low spectral content as shown in Fig. 6b since these flames are not forced and are also thermo-acoustically stable. Hence, these fluctuations arise from the turbulence-chemistry interaction. It is clear from the foregoing discussion that the computational model is able to capture the behaviours of these unforced non-swirling and swirling flames well and hence it is used to investigate the forced flames and characteristics of their FDFs, which are presented in the following subsections.

4.2. Heat release rate response

The FDF obtained from the experiments [32] is shown in Fig. 7. The FDF gain as a function of frequency exhibits a typical behaviour with

Table 1
Strouhal numbers for the three cases studied.

Flame	L_f/D_0	St_1 (40 Hz)	St_1 (160 Hz)	St_2 (40 Hz)	St_2 (160 Hz)
S0	2.4	0.24	0.94	0.21	0.83
S60	1.9	0.19	0.77	0.33	1.33
S60L	1.8	0.18	0.72	0.33	1.33

two local maxima a minimum. For $A = 0.12$ the two maxima are located at 60 and 200 Hz while the minimum is encountered at 160 Hz. For $A = 0.2$, the first maximum remains at 60 Hz, the minimum is shifted to 160 Hz and there is not enough measurements between 200 and 300 Hz to locate the second maximum. The phase, depicted in Fig. 7b, decreases linearly with frequency and shows very little variation with amplitude at all frequencies. This FDF suggests that 40 and 160 Hz are two appropriate frequencies, which are marked using dashed lines in Fig. 7a, to consider for a range of forcing amplitudes to address the objective of this study, specifically to under the effect of swirl on the FDF. The correspondence of those two frequencies to Strouhal Numbers St defined as $St_1 = L_f f/u_0$ [19,31] and $St_2 = \delta_{th} f/s_l$ where δ_{th} is the laminar flame thermal thickness is shown in Table 1.

The measured and computed heat release rate response, the gain and phase of FDF are shown in Fig. 8 for all the three flames, S0, S60 and S60L. These results are shown for 40 and 160 Hz in this
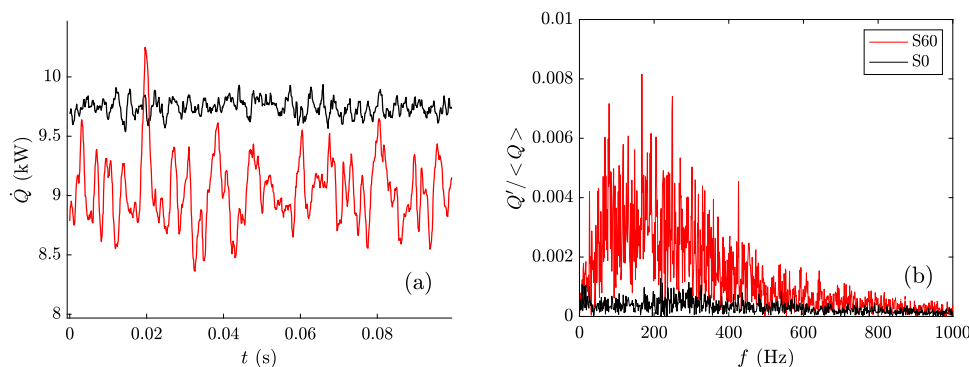
Fig. 6. (a) Time series of volume-integrated heat release rate for cases S0 and S60 and (b) the corresponding fast Fourier Transform.
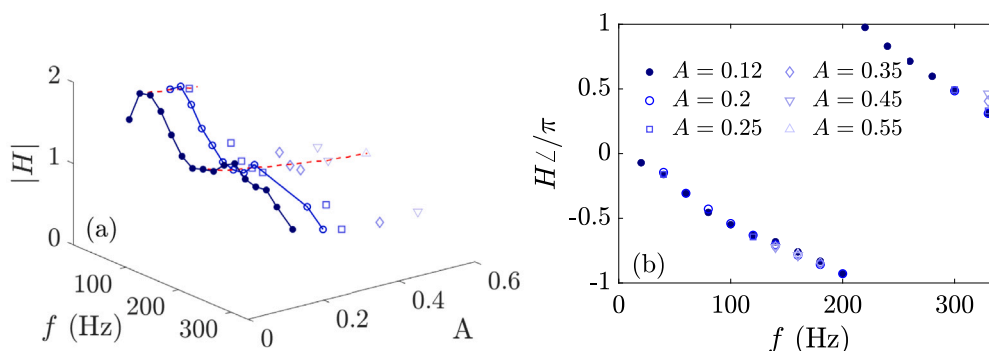

Fig. 7. The full FDF (a) gain and (b) phase obtained experimentally using OH* [32]. The red dashed lines correspond to 40 and 160 Hz. (For interpretation of the references to colour in this figure legend, the reader is referred to the web version of this article.)

figure. The response is mostly linear for the three flames when the forcing frequency is 40 Hz over the range of amplitudes considered. A similar linear behaviour was also reported in [12] for low frequency forcing in a range of non-swirling flames. This is because of the large convective wavelength at low forcing frequency which makes the flame to be convectively compact. This wavelength is about 250 mm at 40 Hz compared to the flame height of about 50 mm. Also, the significant sources of non-linearities such as vortex formation and flame roll-up are absent for this condition [5]. This is also evident from the gain, $|H|$, and phase of the FDF shown in Fig. 8b and c respectively and these two quantities do not seem to vary with A. The heat release rate fluctuations lag the velocity fluctuations at the dump plane by about 0.15π rad. This result also suggests that the swirl (S60) or the size of the flame enclosure (S60L) do not influence the flame response and hence the FDF for 40 Hz forcing frequency.

There are noticeable effects of forcing amplitude at 160 Hz. The flame response in S0 is nonlinear and shows two saturation levels, located at $A \approx 0.2$ and 0.55, as seen in Fig. 8d. Also, the swirl decreases the flame response which does not seem to saturate. However, a past study [23] with smaller blockage ratio, lower swirl number, smaller bulk-mean velocity compared to those considered for this study suggested that the FDF saturated earlier at higher frequencies when the swirl number is increased gradually. This clearly highlights the influences of these parameters on the flame response. The computed and measured gain and phase of the FDF for the three flames considered for this study are also shown in the figure for 160 Hz. The behaviour of gain is consistent with the flame response. The phase for S0 remains constant for amplitudes up to 0.2 and then increases gradually. The phase remains relatively constant for all amplitudes in S60 and S60L and also the enclosure size does not seem to influence the FDF for larger amplitudes. The computed gain agrees quite well with the measurements but there is a substantial difference in the phase, especially for the swirling flames. As explained in Section 3.2, this difference could

arise because for the calculation of the FDF in the experiments, an acoustic velocity derived from a two microphone method is used, while in the simulations, a surfaced averaged axial velocity directly calculated at the dump plane is used. Palies et al. [22] measured the velocity signal using a hotwire upstream of the swirler and LDV at the dump plane and found that even though differences may observed in terms of the absolute values of gain and phase, the trends are unaffected.

For case S60L, a similar behaviour to S60 is apparent, however, a reduction in $Q'/\langle Q \rangle$ is observed for lower forcing amplitudes while they are virtually identical for higher amplitudes $A > 0.35$. This suggests that some saturation occurs at lower forcing amplitudes followed by an increase in flame response. This behaviour is consistent with the observations in [27] for lower swirl number flames. It follows that the use of small enclosure may hinder early saturation by damping the vortex convection, which will be explored further in the next section. In terms of phase, small differences are observed between cases S60 and S60L with a decrease in phase up to $A = 0.25$, followed by a small increase for higher amplitudes.

4.3. Flame dynamics

The instantaneous values of FSD computed through Eq. (10) are used to construct their phase-averaged images for better understanding of the FDF behaviour and influence of swirl, specifically for high forcing frequency, 160 Hz. The results are shown in Figs. 9 and 10 for flame S0 forced at $A = 0.64$ and S60 forced at $A = 0.55$ respectively. The experimental phase averaging has been performed based on the speakers input signal, while the computed is based on the signal of surface averaged axial velocity at the dump plane. Therefore, to compare the sequences, the timings have been shifted so that the flame height is minimum for both computed and measured flames at $\theta = 0°$ in both cases, S0 and S60.
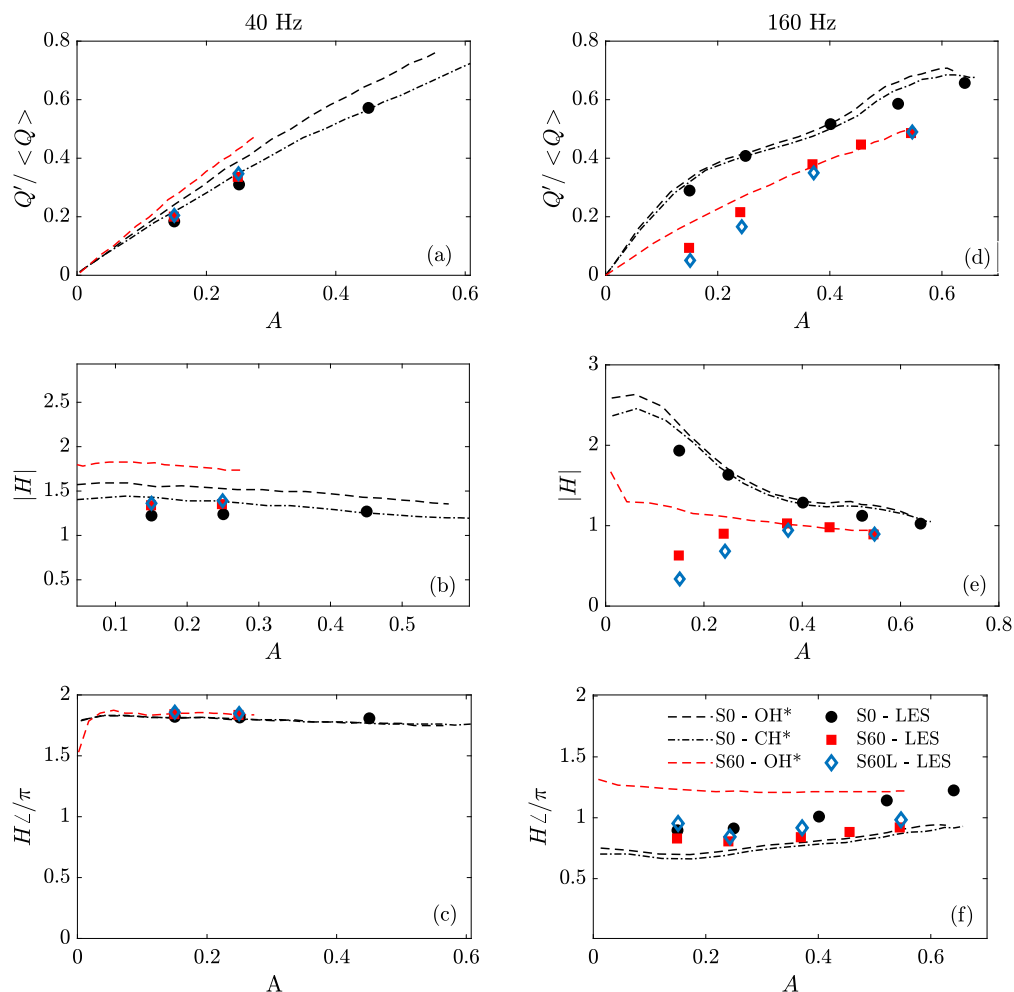
Fig. 8. Comparison of measured, using OH* and CH*, and computed flame responses (top row), the gain (middle row) and phase (bottom row) of the FDF at 40 (left column) and 160 Hz (right column) forcing frequencies. The results are shown for three flames, S0, S60 and S60L, and there are no measurements for S60L. (For interpretation of the references to colour in this figure legend, the reader is referred to the web version of this article.)

The variation of flame height and its roll-up with phase angle captured in the LES compares well with measurements for S0 flame as shown in Fig. 9. The heat release rate is maximum between 180° and 240°, approximately when the flame height is also maximum. Then, a modulation near the flame base causes the flame to collapse creating two counter rotating vortices. The minimum heat release rate is observed at roughly 0° when the flame is the shortest. This behaviour has been observed in previous studies [5,13,14,16].

The flame height varies significantly with phase angle even for swirling flame S60 as shown in Fig. 10. However, the roll-up is quite different (compare Figs. 9 and 10); both the inner and outer flames roll away from the axis in S60 whereas these flame branches roll in opposite directions in S0 flame. This is because of the centrifugal forces arising from the swirling motion which affect the shear layer behaviour. Also, the amount of flame roll-up seen for S60 is lesser than for S0 which is reflected in the minimum flame height at 0° (about 10 to 20 mm for S0 and 20 to 30 mm for S60). This may be happening for three reasons. Firstly, the flame shape is fundamentally different in swirling flows as described in the previous section. The highly corrugated flame with the background vortices arising from swirl may hinder the streamwise flame roll-up compared to the dominant role of thin shear layers and Kelvin–Helmholtz roll-up in non-swirling flames. Secondly, the swirling flame is closer to the combustor wall resulting in considerable flame-wall interaction. Thirdly, the rolled up flame is unable to reach the base as they are influenced strongly by the centrifugal forces arising from the swirling motion, which may lead to flame roll-up in azimuthal

direction as one shall see later. Overall, the agreement between the computed and measured phase-averaged "flame" images are quite good suggesting that the LES model and SGS reaction rate closure used are able to capture the flame dynamics well for the conditions investigated here.

The phase-averaged flame images for the S60L case are shown in Fig. 11. Generally, the behaviour of the flame is very similar to that in S60. It can be observed that the flame looks almost identical to S60 up to 60° and, there is a major difference in the flame shape and behaviour for the phase angle from 120° to 240° (compare Figs. 10 and 11). The convected vortex wraps the flame around as it moves downstream in S60L whereas this is absent in S60 because the vortex and its downstream convection are influenced by the combustor wall since the combustor in S60 is narrower than in S60L. Despite these differences, the flame response in the frequency space $(\dot{Q}'/\langle\dot{Q}\rangle)$, the gain and the phase of the FDF do not seem to be influenced by widening the combustor.

To further understand the effect of swirl and enclosure, the time series of $\dot{Q}'/\langle\dot{Q}\rangle$ is depicted in Fig. 12a and the corresponding Fast Fourier Transforms in Fig. 12b–d. The flame response is delayed in the swirling cases by about 0.6 ms ($\simeq 0.1/f$) compared to the S0 which leads to a lower value for the phase of the FDF as observed in Fig. 8. Furthermore, the peak-to-peak amplitude is relatively lower for the swirling flames compared to the non-swirling case, S0, suggesting that the vortices coming from the swirling motion dampens the flame response at 160 Hz. Some differences can be observed between S60 and
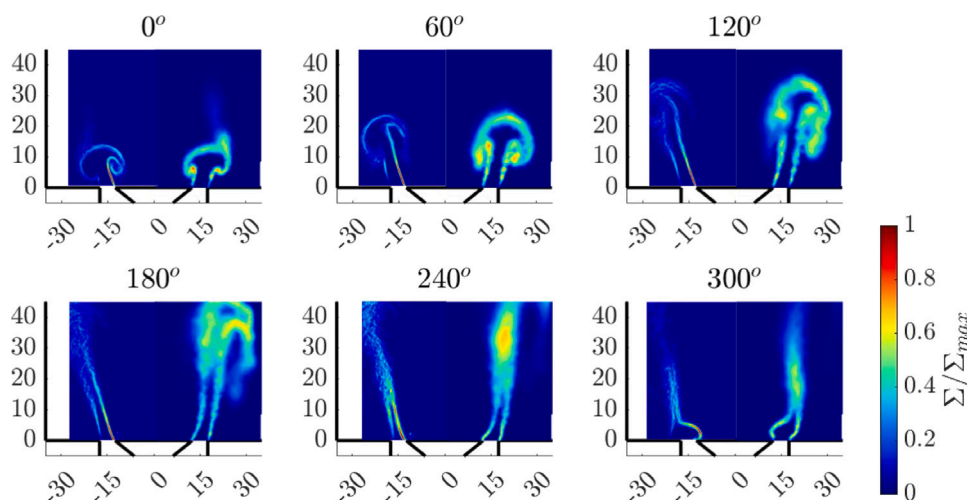
Fig. 9. Phase-averaged images of flame shape for S0 case forced at $A = 0.64$ and 160 Hz. The left halves show experimental results obtained using OH-PLIF while the right halves are from the LES.
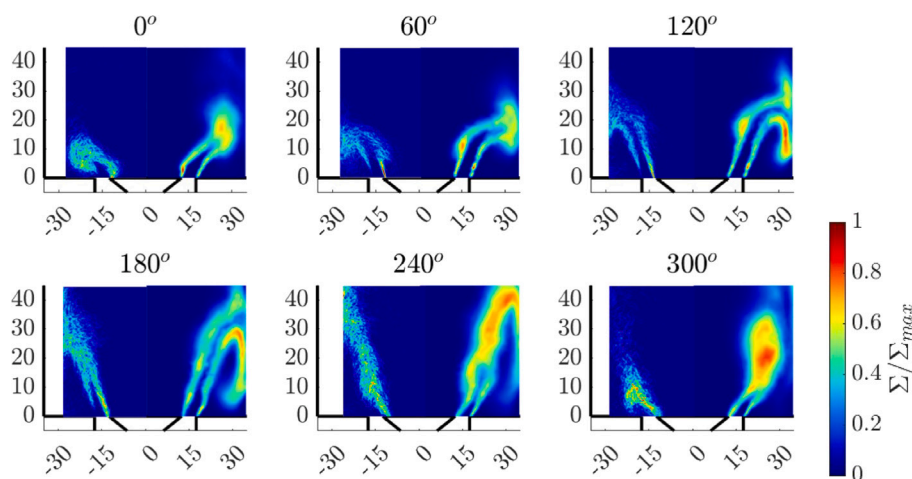

Fig. 10. Phase-averaged images of flame shape for S60 case forced at $A = 0.55$ and 160 Hz. The left halves show experimental results obtained using OH-PLIF while the right halves are from the LES.

S60L but not big enough to change the flame response of FDF. The peak value of $\dot{Q}'/\langle\dot{Q}\rangle$ is slightly lower, but its temporal variation adjusts by itself to yield the same value in the frequency space as it can be seen in Fig. 12c–d. However, for case S60 in Fig. 12c, the first harmonic's magnitude at 320 Hz is 0.15 while for cases S0 and S60L, in Fig. 12b and d, it is 0.1. This suggests that the flame-wall interactions observed in case S60 increase the energy transfer into higher harmonics.

These flame dynamics can also be visualised through a three dimensional iso-contour of $\widetilde{c} = 0.5$. A sequence of these contours at eight different times are shown in Figs. 13, 14, 15, for the cases S0, S60 and S60L respectively. These results are shown for a forcing amplitude of $A = 0.55$ at 160 Hz. These instantaneous snapshots are shown in 3D so that the flame behaviour in the azimuthal direction can also be visualised. The 2D flame roll-up seen in Fig. 9 for the non-swirling flame S0 can also be observed in Fig. 13 which shows the toroidal roll-up yielding a mushroom shape flame in 2D cuts. There is very little azimuthal variation aside from the occasional break up before the flame shortens.

The sequence for S60 shown in Fig. 14 is considerably different. The flame interacts with the wall as its height increases and this causes significant flame breakup as seen to start at instant t_4. This breakup disrupts the flame elongation and vortices travelling along the flame

surface. This flame-wall interaction is absent in S60L case since the flame is quite further away from the combustor wall and hence there are no white contours in Fig. 15. A comparison of this figure to Fig. 14 shows that the S60 and S60L flames are very similar for the period t_1 to t_3 and at t_8. However, the flame behaviour during the period between t_4 to t_7 is quite different for S60 and S60L which is reflected in the temporal variation of heat release rate responses shown in Fig. 12. A closer read of Figs. 14 and 15 shows that the flame rolls-up and wrinkles in the azimuthal direction and this wrinkling also seem to vary with axial distance.

Since the swirling motion introduces azimuthal variation in the flame wrinkling and thus the instantaneous heat release rate, the axial variation of the azimuthal wrinkling suggests that the swirl number (the strength of the swirling motion) changes with downstream distance. Fig. 16 shows the swirl number computed using Eq. (2) at various axial planes in the streamwise direction. The results are shown for both S60 and S60L cases with and without forcing. The forcing amplitude is $A = 0.55$ at $f = 160$ Hz. The unforced cases are shown for two different times (marked as Unforced 1 and Unforced 2 in the figure), 400 ms apart, and these are plotted for reference. The local swirl number, SN_x, is normalised using the time-averaged swirl number at the dump plane for the respective unforced cases and this time-averaged quantity is denoted using $\langle SN_{x=0}\rangle$. Although there is some
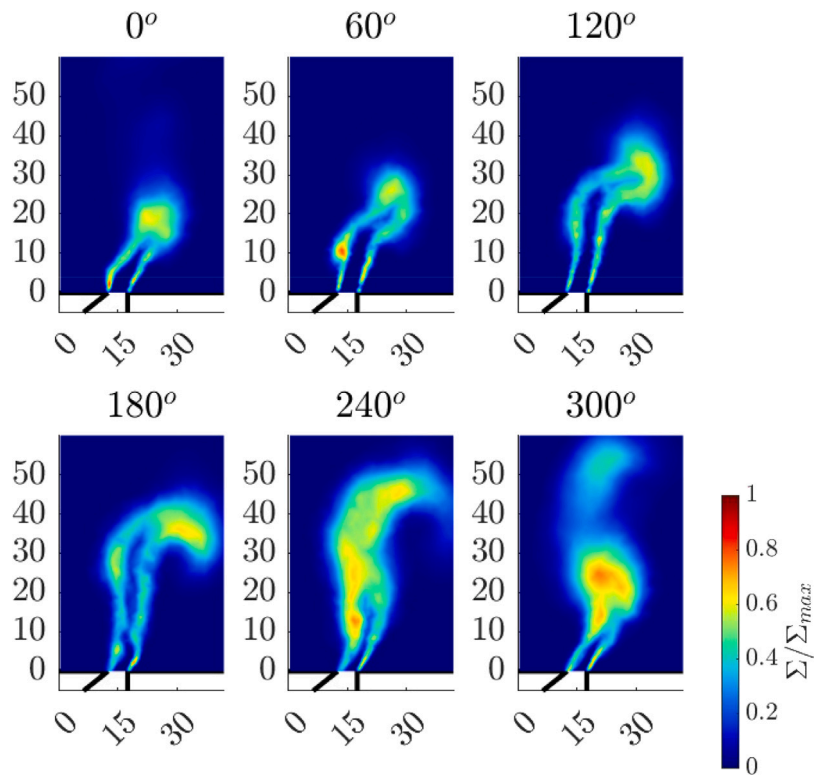
Fig. 11. Phase-averaged images of flame shape for S60L forced at $A = 0.55$ and 160 Hz.
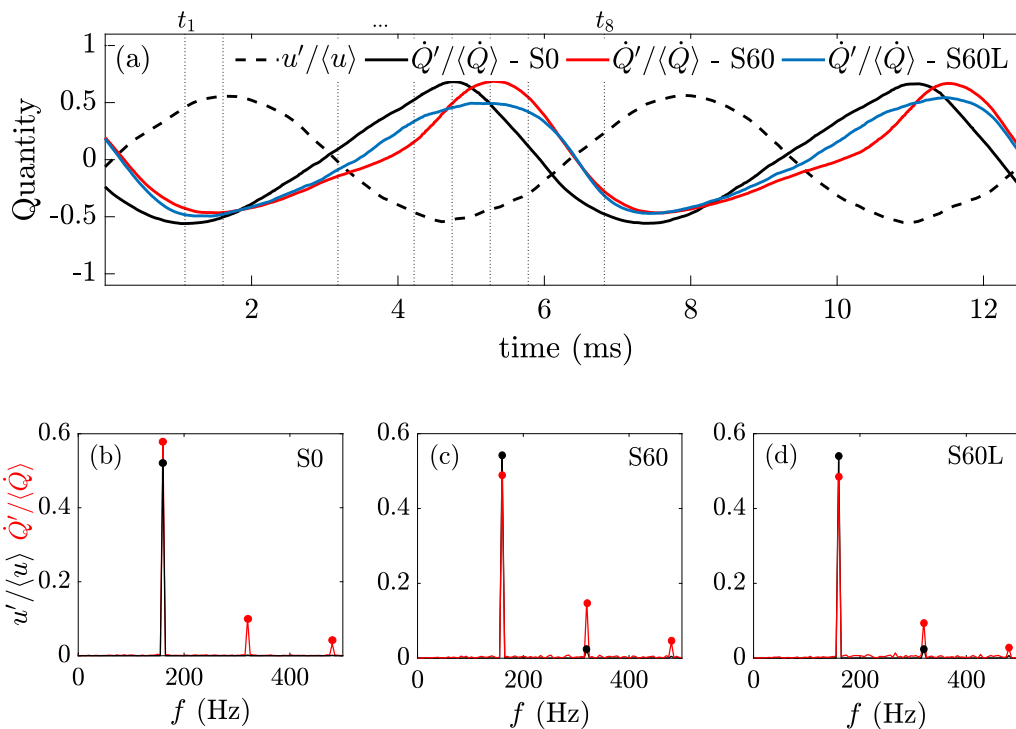

Fig. 12. (a)Temporal variation of $\dot{Q}'/\langle\dot{Q}\rangle$ for $A = 0.55$ and $f = 160$ Hz for the three cases. The variation of $u'/\langle u\rangle$ at the dump plane is also shown for comparison. The corresponding Fast Fourier Transforms for the three cases are shown in (b) to (d).

variation of the normalised SN_x with x/L, where L is the combustor height, there is almost no change in this swirl number with time for the unforced cases. However, SN_x varies significantly both in time and space as depicted in Fig. 16 for the forced cases. Even in the dump plane there is $\pm50\%$ change over a forcing cycle period compared to the unforced case. Although the pattern of spatio-temporal variations of $SN_x/\langle SN_{x=0}\rangle$ looks similar for S60 and S60L cases, the local values are quite different yielding quite different flame shapes and dynamics.
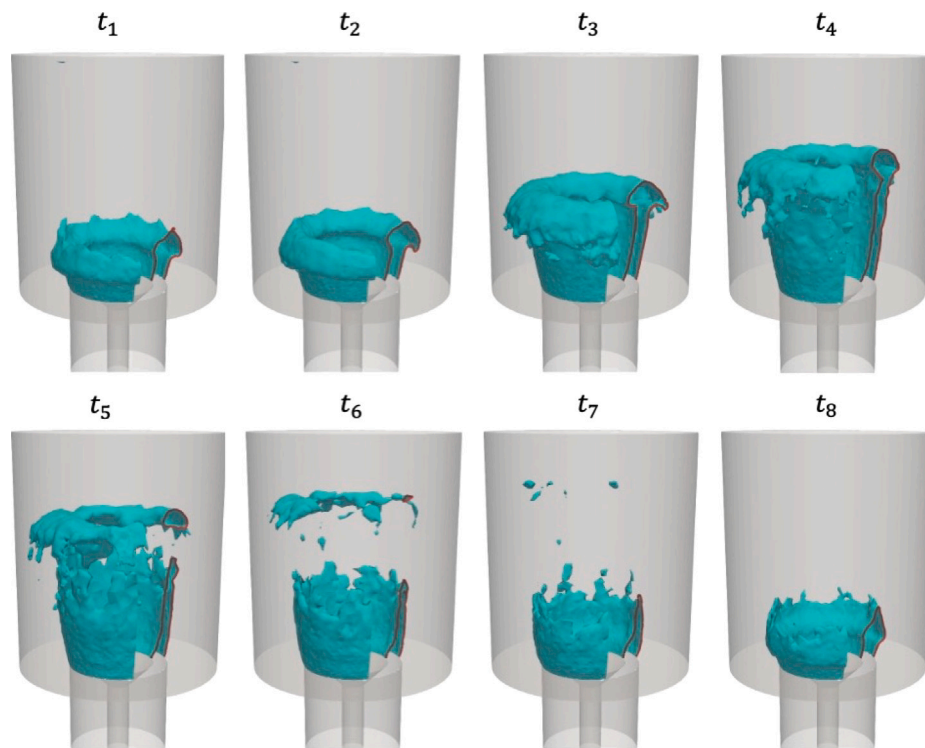
Fig. 13. Snapshots of $\tilde{c} = 0.5$ iso-surface at the eight instants for case S0. These eight times are marked using dotted lines in Fig. 12. The red contours represent the 2D cuts. (For interpretation of the references to colour in this figure legend, the reader is referred to the web version of this article.)
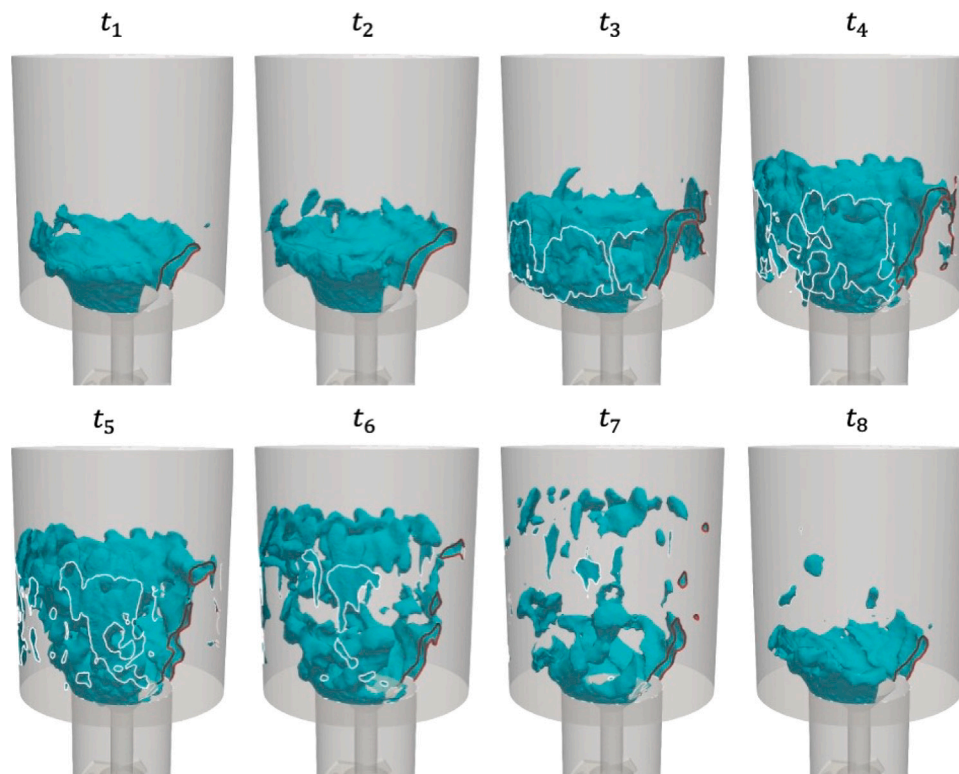

Fig. 14. Snapshots of $\tilde{c} = 0.5$ iso-surface at the eight instants for case S60. These eight times are marked using dotted lines in Fig. 12. The red contours represent the 2D cuts and the white lines represent the interaction with the combustor wall. (For interpretation of the references to colour in this figure legend, the reader is referred to the web version of this article.)
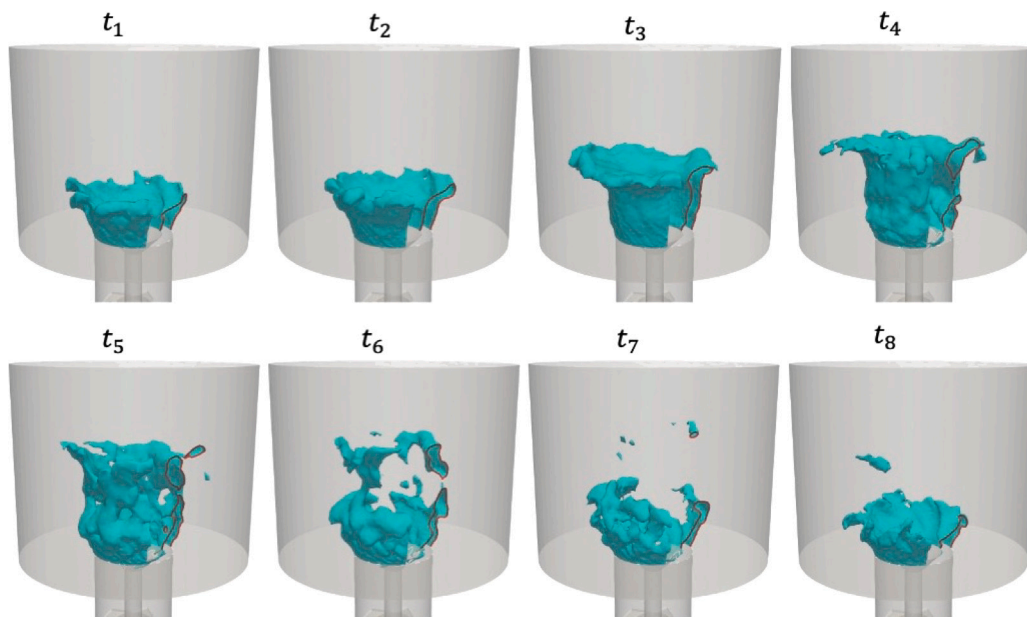
Fig. 15. Snapshots of $\tilde{c} = 0.5$ iso-surface at the eight instants for case S60L. These eight times are marked using dotted lines in Fig. 12. The red contours represent the 2D cuts. (For interpretation of the references to colour in this figure legend, the reader is referred to the web version of this article.)
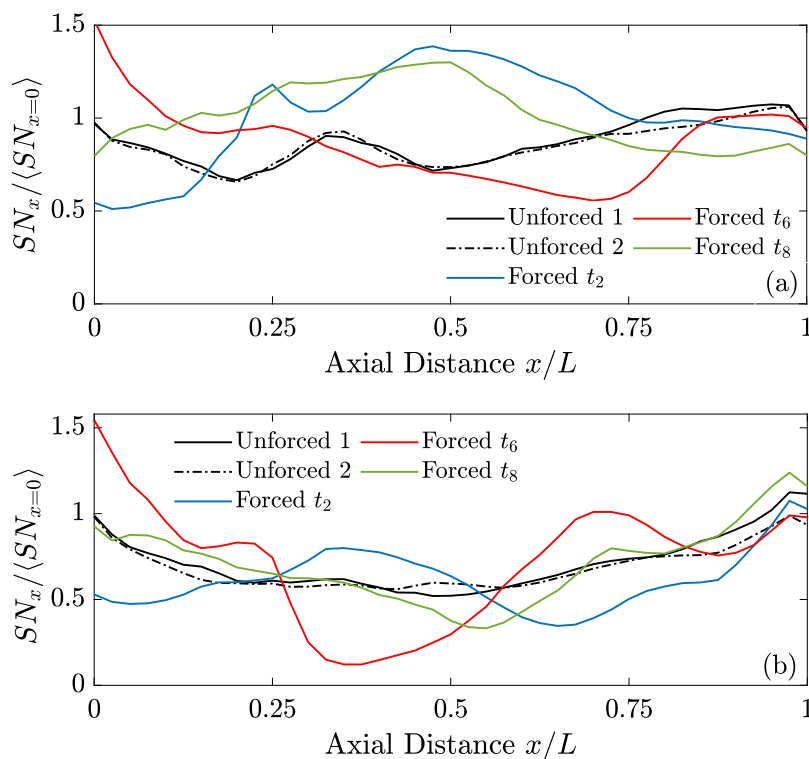

Fig. 16. The variation of normalised swirl number, $SN_x/\langle SN_{x=0}\rangle$, along the combustor height. The results are shown for (a) S60 and (b) S60L with and without forcing. The time t_i shown above are marked in Fig. 12. The two signals for the unforced cases are 400 ms apart. (For interpretation of the references to colour in this figure legend, the reader is referred to the web version of this article.)

Hence, the swirling flames and their response to forcing, specifically at larger amplitudes and frequencies, are complex which can alter the non-linear characteristics of the flame response and therefore, affect saturation.

5. Conclusion

Turbulent lean premixed ethylene-air flames stabilised behind a conical bluff body are studied under non-swirling and highly swirling

conditions in this work, to understand the flame dynamics and the effect of swirl on the FDF. The influence of combustor size is also investigated by enlarging the cylindrical combustor. The subgrid scale combustion in the LES model is modelled using a presumed probability density function based approach [38,40,41]. The computational model is validated using measured flame shapes and velocity statistics and the agreement with measurement is observed to be very good. Two frequencies, low (40 Hz) and high (160 Hz) are considered for detailed investigation corresponding to Strouhal numbers 0.21 and 0.83 based on the flame timescale for the non-swirling flame (0.33 and 1.32 for the swirling flames).

At 40 Hz, both the swirling and non-swirling flames produced a very similar response with limited saturation because of the large convective wavelength which makes the flame to oscillate in the streamwise direction and not roll up. The agreement between the computed and measured FDF gain and phase is observed to be very good for all cases. The enclosure size does not seem to influence these quantities unduly.

At 160 Hz, the non-swirling flame appears to be saturated at forcing amplitudes larger than 0.55, however, the swirling flames show a linear behaviour and smaller heat release rate fluctuations for the range of forcing amplitudes considered. With the larger enclosure, the swirling flame produced a smaller gain at smaller amplitudes. Some differences are observed between measured and computed heat release rate amplitude for smaller forcing amplitudes. This also reflects in the FDF gain and phase.

An examination of the phase averaged images shows some fundamental differences in the flame roll-up mechanisms between the swirling and non-swirling flames. This is attributed to the highly corrugated nature of the swirling flames and the flame to roll-up in the azimuthal direction. The azimuthal roll-up is found to be linked to the large spatio-temporal variations of the swirl number during the forcing cycle. In the case with the narrow enclosure, the presence of the wall has been found to interrupt the vortex formation breaking up the flame. These behaviours ultimately lead to changes in the non-linear characteristics of the flame. This line of analysis should be extended to a wider range of conditions including more forcing frequencies and equivalence ratios to study the full FDF of a swirling flame and this will be considered in a future work.

CRediT authorship contribution statement

Dimitrios P. Kallifronas: Performed the simulations, Conceptualised the computational work and analysis, Wrote the original draft, Reviewed and edited the manuscript. **James C. Massey:** Assisted with the simulations, Conceptualised the computational work and analysis, Reviewed and edited the manuscript. **Zhi X. Chen:** Assisted with the simulations, Conceptualised the computational work and analysis, Reviewed and edited the manuscript. **Ramanarayanan Balachandran:** Conceptualised the experimental methodology, investigation and analysis, Reviewed and edited the manuscript. **Nedunchezhian Swaminathan:** Responsible for supervision and acquiring funding for Cambridge authors, Conceptualised the computational work and analysis, Reviewed and edited the manuscript.

Declaration of competing interest

The authors declare that they have no known competing financial interests or personal relationships that could have appeared to influence the work reported in this paper.

Data availability

Data may be obtained by contacting the corresponding author.

References

[1] Dowling AP, Stow SR. J Propuls Power 2003;19(5):751–64. http://dx.doi.org/10.2514/2.6192.
[2] Stow SR, Dowling AP. J Eng Gas Turbines Power 2009;131(3). http://dx.doi.org/10.1115/1.2981178.
[3] Han X, Li J, Morgans AS. Combust Flame 2015;162(10):3632–47. http://dx.doi.org/10.1016/j.combustflame.2015.06.020.
[4] Schuller T, Durox D, Candel S. Combust Flame 2003;134(1–2):21–34. http://dx.doi.org/10.1016/S0010-2180(03)00042-7.
[5] Balachandran R, Ayoola B, Kaminski C, Dowling A, Mastorakos E. Combust Flame 2005;143(1):37–55. http://dx.doi.org/10.1016/j.combustflame.2005.04.009.
[6] Fleifil M, Annaswamy A, Ghoneim Z, Ghoniem A. Combust Flame 1996;106(4):487–510. http://dx.doi.org/10.1016/0010-2180(96)00049-1.
[7] Dowling AP. J Fluid Mech 1997;346:271–90. http://dx.doi.org/10.1017/S0022112097006484.
[8] Dowling AP. J Fluid Mech 1999;394:51–72. http://dx.doi.org/10.1017/S0022112099005686.
[9] Peracchio AA, Proscia WM. J Eng Gas Turbines Power 1999;121(3):415–21. http://dx.doi.org/10.1115/1.2818489.
[10] Stow SR, Dowling AP. Turbo Expo: Power Land Sea Air 2004;775–86. http://dx.doi.org/10.1115/GT2004-54245.
[11] Noiray N, Durox D, Schuller T, Candel S. J Fluid Mech 2008;615:139–67. http://dx.doi.org/10.1017/S0022112008003613.
[12] Durox D, Schuller T, Noiray N, Candel S. Proc Combust Inst 2009;32(1):1391–8. http://dx.doi.org/10.1016/j.proci.2008.06.204.
[13] Armitage C, Balachandran R, Mastorakos E, Cant R. Combust Flame 2006;146(3):419–36. http://dx.doi.org/10.1016/j.combustflame.2006.06.002.
[14] Ruan S, Dunstan TD, Swaminathan N, Balachandran R. Combust Sci Technol 2016;188(7):1115–35. http://dx.doi.org/10.1080/00102202.2016.1174117.
[15] Han X, Morgans AS. Combust Flame 2015;162(5):1778–92. http://dx.doi.org/10.1016/j.combustflame.2014.11.039.
[16] Lee CY, Cant RS. Flow Turbul Combust 2017;99:461–86. http://dx.doi.org/10.1007/s10494-017-9811-4.
[17] Cheng Y, Luo K, Jin T, Li Z, Wang H, Fan J. AIP Adv 2021;11(1):015236. http://dx.doi.org/10.1063/5.0029904.
[18] Hirsch C, Fanaca D, Reddy P, Polifke W, Sattelmayer T. ASME Turbo Expo 2005: Power Land Sea Air 2005;151–60. http://dx.doi.org/10.1115/GT2005-68195.
[19] Komarek T, Polifke W. J Eng Gas Turbines Power 2010;132(6):061503. http://dx.doi.org/10.1115/1.4000127.
[20] Kim KT, Santavicca DA. Combust Sci Technol 2013;185(7):999–1015. http://dx.doi.org/10.1080/00102202.2012.752734.
[21] Dupuy F, Gatti M, Mirat C, Gicquel L, Nicoud F, Schuller T. Combust Flame 2020;217:222–36. http://dx.doi.org/10.1016/j.combustflame.2020.03.026.
[22] Palies P, Durox D, Schuller T, Candel S. Combust Flame 2010;157(9):1698–717. http://dx.doi.org/10.1016/j.combustflame.2010.02.011.
[23] Palies P, Durox D, Schuller T, Candel S. Combust Sci Technol 2011;183(7):704–17. http://dx.doi.org/10.1080/00102202.2010.538103.
[24] Krediet HJ, Beck CH, Krebs W, Schimek S, Paschereit CO, Kok JB. Combust Sci Technol 2012;184(7–8):888–900. http://dx.doi.org/10.1080/00102202.2012.663981.
[25] Gatti M, Gaudron R, Mirat C, Zimmer L, Schuller T. Proc Combust Inst 2019;37(4):5197–204. http://dx.doi.org/10.1016/j.proci.2018.06.148.
[26] Bellows BD, Bobba MK, Forte A, Seitzman JM, Lieuwen T. Proc Combust Inst 2007;31(2):3181–8. http://dx.doi.org/10.1016/j.proci.2006.07.138.
[27] Liu W, Xue R, Zhang L, Yang Q, Wang H. Combust Flame 2022;235:111733. http://dx.doi.org/10.1016/j.combustflame.2021.111733.
[28] Rajendram-Soundararajan P, Durox D, Renaud A, Vignat G, Candel S. Combust Flame 2022;238:111947. http://dx.doi.org/10.1016/j.combustflame.2021.111947.
[29] Tay-Wo-Chong L, Polifke W. J Eng Gas Turbines Power 2013;135(2):021502. http://dx.doi.org/10.1115/1.4007734.

[30] Cuquel A, Durox D, Schuller T. Proc Combust Inst 2013;34(1):1007–14. http://dx.doi.org/10.1016/j.proci.2012.06.056.

[31] De Rosa AJ, Peluso SJ, Quay BD, Santavicca DA. J Eng Gas Turbines Power 2016;138(6). http://dx.doi.org/10.1115/1.4031885, 061507.

[32] Balachandran R. Experimental investigation of the response of turbulent pre-mixed flames to acoustic oscillations (Ph.D. thesis), (May). University of Cambridge; 2005.

[33] Beer JM, Chigier NA. Combustion aerodynamics. New York: Wiley; 1972.

[34] Germano M, Piomelli U, Moin P, Cabot WH. Phys Fluids A: Fluid Dyn 1991;3(7):1760–5. http://dx.doi.org/10.1063/1.857955.

[35] Lilly DK. Phys Fluids A: Fluid Dyn 1992;4(3):633–5. http://dx.doi.org/10.1063/1.858280.

[36] Bilger RW. Symp (Int) Combust 1989;22(1):475–88. http://dx.doi.org/10.1016/S0082-0784(89)80054-2.

[37] Pitsch H, Steiner H. Phys Fluids 2000;12(10):2541–54. http://dx.doi.org/10.1063/1.1288493.

[38] Chen ZX, Ruan S, Swaminathan N. Proc Combust Inst 2017;36(2):1645–52. http://dx.doi.org/10.1016/j.proci.2016.06.023.

[39] Dunstan TD, Minamoto Y, Chakraborty N, Swaminathan N. Proc Combust Inst 2013;34(1):1193–201. http://dx.doi.org/10.1016/j.proci.2012.06.143.

[40] Ruan S, Swaminathan N, Darbyshire O. Combust Theor Model 2014;18(2):295–329. http://dx.doi.org/10.1080/13647830.2014.898409.

[41] Langella I, Swaminathan N. Combust Theor Model 2016;20(3):410–40. http://dx.doi.org/10.1080/13647830.2016.1140230.

[42] Massey JC, Chen ZX, Swaminathan N. Flow Turbul Combust 2021;106(4):1355–78. http://dx.doi.org/10.1007/s10494-020-00192-4.

[43] Goodwin DG, Moffat HK, Speth RL. Cantera: an object-oriented software toolkit for chemical kinetics, thermodynamics, and transport processes. 2017, URL www.cantera.org.

[44] Wang H, Laskin A. A comprehensive kinetic model of ethylene and acetylene oxidation at high temperatures. Technical report, University of South California; 1998, URL http://ignis.usc.edu/Mechanisms/C2-C4/c2.pdf.

[45] Massey JC, Langella I, Swaminathan N. Flow Turbul Combust 2018;101(4):973–92. http://dx.doi.org/10.1007/s10494-018-9948-9.

[46] Kallifronas DP, Ahmed P, Massey JC, Talibi M, Ducci A, Balachandran R, Swaminathan N, Bray KNC. Combust Sci Technol 2022. http://dx.doi.org/10.1080/00102202.2022.2041616.

[47] Lee CY, Cant RS. Flow Turbul Combust 2017;98:155–76. http://dx.doi.org/10.1007/s10494-016-9751-4.